ARTICLE IN PRESS

Ceramics International xxx (xxxx) xxx

Contents lists available at ScienceDirect

Ceramics International

journal homepage: www.elsevier.com/locate/ceramint

Photoluminescence properties of Pr-doped $LaAsO_4$: An experimental and theoretical study employing density functional theory

Basma Marzougui [a], Youssef Ben Smida [a,*], Mounir Ferhi [b], Hela Ferjani [c], Damian Onwudiwe [d,e], Ahmed Hichem Hamzaoui [a], Mohamed Triki [a], Y. Al Douri [f,g]

[a] Centre National de Recherches en Sciences des Matériaux, Laboratoire de Valorisation des Matériaux Utiles, Technopôle Borj Cedria, BP 73, 8027, Soliman, Tunisia
[b] Centre National de Recherches en Sciences des Matériaux, Laboratoire de Physico-Chimie des Matériaux Minéraux et leurs Applications, Technopôle Borj Cedria, BP 73, 8027, Soliman, Tunisia
[c] Deparment of Chemistry, College of Science, Imam Mohammad Ibn Saud Islamic University (IMSIU), Riyadh, 11623, Kingdom of Saudi Arabia
[d] Department of Chemistry, School of Physical and Chemical Science, Faculty of Natural and Agricultural Sciences, Mafikeng Campus, North-West University, Private Bag X2046, Mmabatho, 2735, South Africa
[e] Material Science Innovation and Modelling (MaSIM) Research Focus Area, Faculty of Natural and Agricultural Sciences, Mafikeng Campus, North-West University, Private Bag X2046, Mmabatho, 2735, RSA, South Africa
[f] Department of Mechanical Engineering, Faculty of Engineering, Piri Reis University, Eflatun Sk. No:8, 34940, Tuzla, Istanbul, Turkey
[g] Nanotechnology and Catalysis Research Center (NANOCAT), University of Malaya, Kuala Lumpur, Malaysia

ARTICLE INFO

Handling Editor: Dr P. Vincenzini

Keywords:
Praseodymium
Ternary metal oxide
Bond structure
Density of states
Dielectric function
Photoluminescence

ABSTRACT

Praseodymium doped lanthanum arsenate, denoted as $La_{1-x}Pr_xAsO_4$, has been synthesized with different concentrations of the dopant (x = 0.5 %; 1 %; 2 %; 3 % and 5 %) via the combustion method and their optoelectronic properties have been investigated. A study of the crystalline structure and size of the compound by XRD confirms that both the pristine $LaAsO_4$ and Pr-doped $LaAsO_4$ are pure and maintain a monoclinic crystal structure, with the crystalline size ranging from 60 to 76 nm. The morphological study of the nanoparticles by SEM analysis reveals that all samples, regardless of the concentration of Pr^{3+}, consist of homogeneously packed and irregularly shaped small particles. The optical studies by absorption and fluorescence spectroscopies highlight the unique optoelectronic characteristics of $La_{1-x}Pr_xAsO_4$, with absorption predominantly in the UV and blue regions and prominent emission peaks in the visible spectrum, most notably at 610 nm. The optimal luminescence is observed at a 0.5 % Pr^{3+} doping level, deviating from typical trends as higher concentrations lead to diminished emission intensity and lifetime due to concentration quenching effects. The application of Density Functional Theory (DFT) with GGA + PBE and GGA + PBE + U approximations has effectively elucidated the electronic structure and optical properties of the Pr-doped $LaAsO_4$. The incorporation of Pr's 4f states within the $LaAsO_4$ forbidden band significantly alters the material's electronic landscape, notably reducing the optical band gap from 4.45 eV to 2.299 eV. This modification in the band structure aligns favourably with the dielectric function curves and density of states analyses, corroborating the observed visible light emission in the doped samples.

1. Introduction

The rare earth metal oxides such as $LnXO_4$ (Ln = rare earth and X = As, P, or V), have received considerable attention for their interesting properties and potential technological applications, especially in the areas of protonic conductivity and photoluminescence [1–10]. Among them, $LaPO_4$ and $LaVO_4$ have been extensively studied and well-recognized for their performances in these applications. However, the arsenate analogue, lanthanum ortho-arsenates ($LaAsO_4$), is relatively less explored. Only limited studies are available on $LaAsO_4$, such as the study on the mechanisms of proton transport in undoped and Sr-doped $LaAsO_4$ [11,12], and Eu-doped $LaAsO_4$ where only the red emission process has been studied [13,14].

Praseodymium (Pr) is exceptionally appealing among rare earth elements, owing to its proficiency in emitting across the visible light range. Its diverse electronic transitions, particularly those leading to vibrant red emissions, are leveraged in several industry-praised materials. For instance, Pr-doped yttrium aluminium garnet (YAG: Pr) [15,

* Corresponding author.
E-mail address: Youssef.bensmida@cnrsm.rnrt.tn (Y. Ben Smida).

https://doi.org/10.1016/j.ceramint.2024.04.370
Received 11 February 2024; Received in revised form 17 April 2024; Accepted 26 April 2024
Available online 27 April 2024

16] is extensively explored and reported for its use in solid-state lasers and lighting applications due to its notable efficiency and colour rendering.

In this context, the photoluminescence (PL) properties of Pr-doped $LaPO_4$ orthophosphates are characterized by distinct excitation and emission spectra [17,18]. The excitation monitored at 607 nm revealed sharp bands corresponding to $^3H_4 \rightarrow {}^3P_0$, $^3P_1$, $^1I_6$, and $^3H_4 \rightarrow {}^3P_2$ transitions, with additional weak bands suggesting that crystallization conditions affect phonon interactions. The emission spectra display dominant bands for the $^3P_0 \rightarrow {}^3H_4$ and $^1D_2 \rightarrow {}^3H_4$ transitions with several narrow lines. For Pr-doped $LaVO_4$ [19,20], when it was excited at 315 nm, it exhibited emission bands corresponding to the $^3P_0 \rightarrow {}^3H_{4,5,6}$, $^1D_2 \rightarrow {}^3H_4$, and $^3P_0 \rightarrow {}^3F_2$ electron transitions of the Pr^{3+} ion. Notably, the emission intensity of these bands is not directly proportional to the dopant concentration, with the highest emission peak observed at lower concentrations, suggesting an optimal doping level exists for achieving maximum luminescence efficiency. The chromaticity coordinates (CIE) displayed a shift from blue to white and then to light-green regions [20, 21] as the Pr^{3+} ion concentration was adjusted, highlighting the tunability of the emission colour. This photoluminescence characteristic is further influenced by crystal field effects, which causes a shift in the energy states of Pr^{3+}, particularly the $^4f-{}^5d_1$ transition, thereby affecting the emission intensity and chromaticity [22]. The findings suggested that by fine-tuning the Pr^{3+} ion concentration, a single white-light-emitting phosphor with desired luminescent properties could be developed [23].

Despite the well-documented applications of rare earth-doped materials in photoluminescence, the unique aspects of Pr-doped $LaAsO_4$, particularly in arsenate hosts, remain underexplored compared to more commonly studied systems like phosphates and vanadates. This gap in research highlights an opportunity to explore the specific behavior of Pr^{3+} within an arsenate matrix, with potential implications for tuning optical properties through targeted dopant concentrations. The enhanced understanding of Pr's electron transitions within $LaAsO_4$ could pave the way for novel applications in optoelectronics and photonics, where tailored luminescent properties are crucial. In this sense, our work aims to study the effect of Pr^{3+} concentration on the PL properties of Pr-doped $LaAsO_4$. The samples were prepared using the combustion method, a technique chosen for its efficiency to maintain the purity and structural integrity of compounds. Further, the microstructural properties of the metal oxides were thoroughly examined using SEM and the Debye-Scherrer method to ensure a comprehensive understanding of the material's morphology and crystal structure.

To deepen our insights into the electronic and optical properties of $LaAsO_4$, a computational method employing Density Functional Theory (DFT) was utilized. This approach facilitates a more understanding of how praseodymium incorporation affects the material properties by demonstrating the potential of DFT to predict and explain the PL behavior.

2. Experimental and computational methods

Both undoped and Pr-doped $LaAsO_4$ compounds were prepared using the combustion method. La_2O_3, Pr_6O_{11} and As_2O_5 (Sigma Aldrich, >99 %) were used as reagents. Firstly, an appropriate amount of La_2O_3 and Pr_6O_{11} was dissolved in nitric acid under vigorous stirring for few minutes using a hotplate. Further, $NH_4H_2AsO_4$ (prepared from As_2O_3 at the Laboratory) was dissolved in hot deionized water and added to the solution. After mixing the two solutions, 0.4 g of glycine was added and then heated until the combustion. Finally, the obtained powder was grinded and calcined in a muffle furnace at 900 °C for 2 h [24,25].

The powder X-ray diffraction (PXRD) patterns were obtained at room temperature using a D8 Bruker Advance diffractometer equipped with a Cu anticathode (CuKα radiation λ = 1.54056 Å). The measurements were performed in the 10–80° range under Bragg–Brentano geometry with step 0.02° and counting time of 2s per step. The cell parameters were obtained using the refinement of the computer program X'Pert high score plus.

The microstructure and morphology of the compound were studied using the scanning electron microscopy (SEM) and Debye-Scherrer method. The SEM measurement was performed by Quanta 650 from the FEI microscope. The photoluminescence (PL) property and decay times of Pr-doped $LaAsO_4$ were investigated using a fluorescence spectrometer (Edinburgh Instrument FS5) with a 150 W continuous and pulsed Xenon lamp as a light source at room temperature.

The electronic structure and optical properties of the pristine and Pr-doped $LaAsO_4$ were explored using the density functional theory (DFT), which was carried out using the CASTEP code [26]. For the pristine $LaAsO_4$, we have used the GGA-PBE [27,28] approximation, and crystallographic data with ICSD (Inorganic crystal structure database) number 155917 has been used as starting set. In the case of the Pr-doped $LaAsO_4$, due to the limitation of the computer to work on one unit cell only, the calculation on $La_{0.75}Pr_{0.25}AsO_4$ was performed by the replacement of one Lanthanum by a Praseodymium element. The DFT calculation of $La_{0.75}Pr_{0.25}AsO_4$ structure has been performed using the GGA-PBE + U. The Hubbard parameter U was fixed at 4 eV to describe the correlation effects in localized d orbital for Pr atom [29–31].

For the two structures, the calculations have been performed for a 500-eV cutoff energy and 6 × 5 × 5 K-point. The convergence criteria include the atomic force, maximum displacement, and total energy, which are calculated to give 0.05 Å, 0.002 eV $Å^{-1}$ and 10^{-6} eV, respectively. The ground state of the two compounds were obtained by the minimization of energy using the BFGS (Broyden-Fletcher-Goldfarb-Shannon) algorithm [32].

3. Results and discussion

3.1. Structural properties

Fig. 1a shows the XRD pattern of the undoped $LaAsO_4$. The indexed peaks correspond to the monoclinic crystal structure of $LaAsO_4$. It is characterized by the $P2_1/n$ space group (No. 14) and aligns closely with the standard PDF number 00-015-0756. This standard denotes a unit cell with dimensions a = 7.0078 Å, b = 7.2120 Å, c = 6.7670 Å, and an angle β = 104.5°. Conversely, Fig. 1b illustrates the XRD patterns of the Pr doped $LaAsO_4$ samples. The consistency across all diffraction patterns, coupled with the absence of extraneous peaks, confirms the high purity of the synthesized powders.

3.2. Microstructural study

The crystallite size was determined by means of XRD line broadening method using the Debye-Scherrer equation:

$$\mathbf{D} = \frac{\mathbf{0.9} * \boldsymbol{\lambda}}{\boldsymbol{\beta} * \mathbf{cos}\,\theta} \quad (1)$$

where, λ is the wavelength of XRD (λ = 1.54 Å for CuKα), β is broadening of the diffraction line measured at half of its maximum intensity (FWHM: full width at half maximum), θ is the Bragg's diffraction angle and D is the crystallite size.

The average crystallite sizes of different $LaAsO_4:Pr^{3+}$ is about 65 nm as displayed in Table 1.

Fig. 2 presents the SEM micrographs of the $La_{1-x}Pr_xAsO_4$. It indicates the presence of irregular small particles, which consist of homogeneous and almost identical particles. There are no clear patterns of ordering or arrangement as the concentration of the dopant increases.

In the synthesis of Pr-doped $LaAsO_4$ via the combustion method, the uniformity in particle size and morphology is achieved as evidenced by SEM and XRD analyses. In fact, the pure monoclinic crystal structure is maintained across varying Pr concentrations, which underlines the efficiency of the synthesis method. The crystallite sizes, calculated using

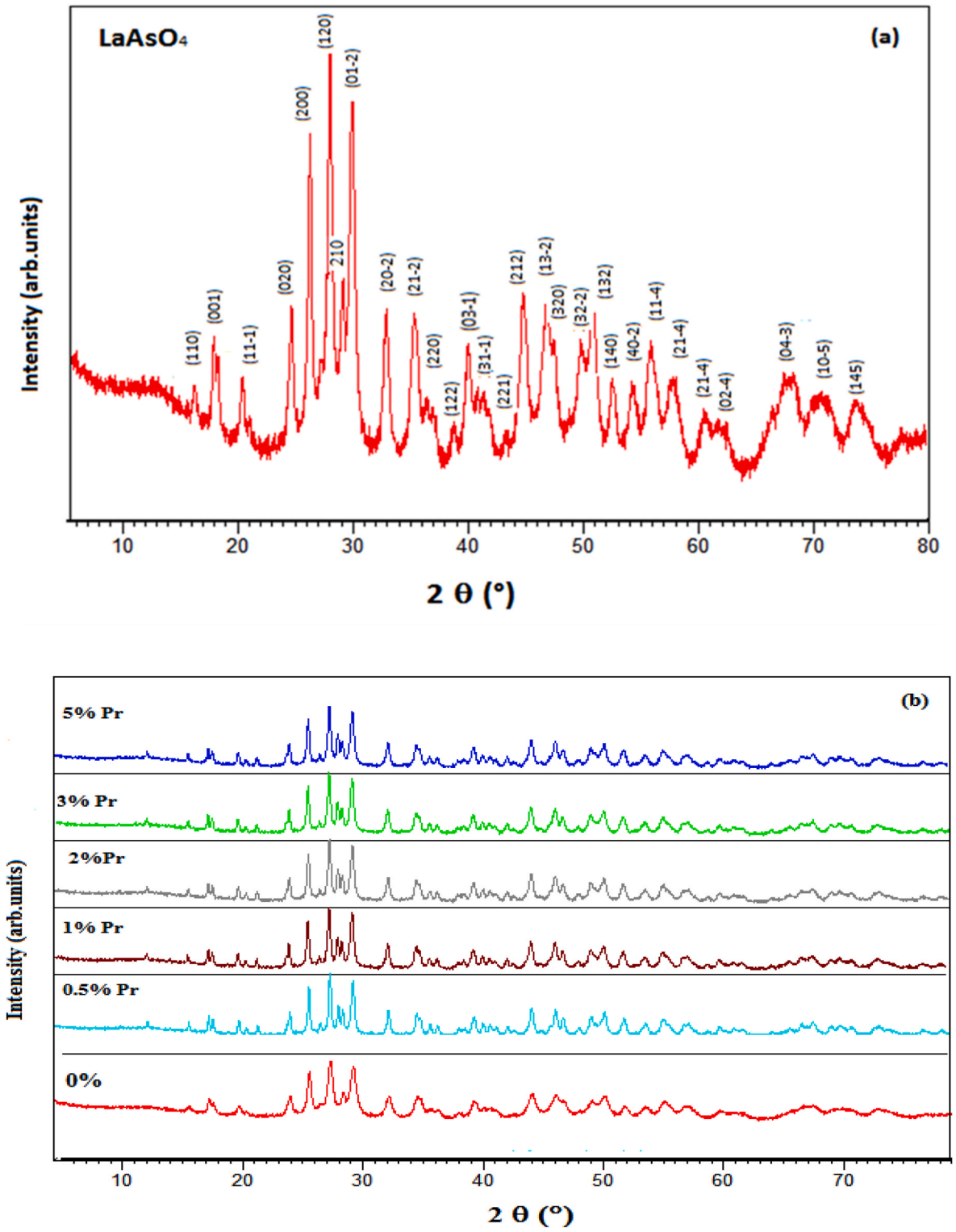

Fig. 1. XRD patterns of (a) $LaAsO_4$ and (b) $La_{1-x}Pr_xAsO_4$ (x = 0.5 %, 1 %, 2 %, 3 %, 5 %).

Table 1
Crystallite sizes of $La_{1-x}Pr_xAsO_4$ (x = 0 %, 0.5 %, 1 %, 2 %, 3 %, 5 %) powders measured by the Debye-Scherrer equation.

Pr^{3+} (%)	0	0.5	1	2	3	5
D (nm)	60	76	75	64	67	63

the Debye-Scherrer equation from XRD data, ranged consistently, indicating a controlled nucleation and growth processes influenced by Pr doping, which is crucial especially for applications requiring uniform optical properties.

3.3. Luminescence study of Pr-doped $LaAsO_4$

The room temperature PL excitation spectra, registered at $\lambda_{em} = 618$ nm of $La_{1-x}Pr_xAsO_4$ are shown in Fig. 3. The high-pitched lines in the

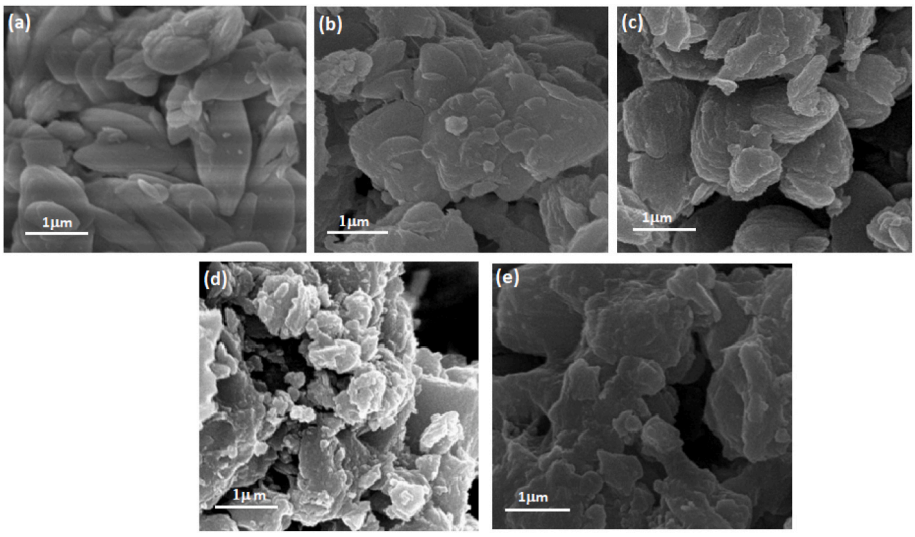

Fig. 2. SEM micrographs of $La_{1-x}Pr_xAsO_4$ (x = 0.5 % (a); 1 % (b); 2 % (c); 3 % (d) and 5 % (e)).

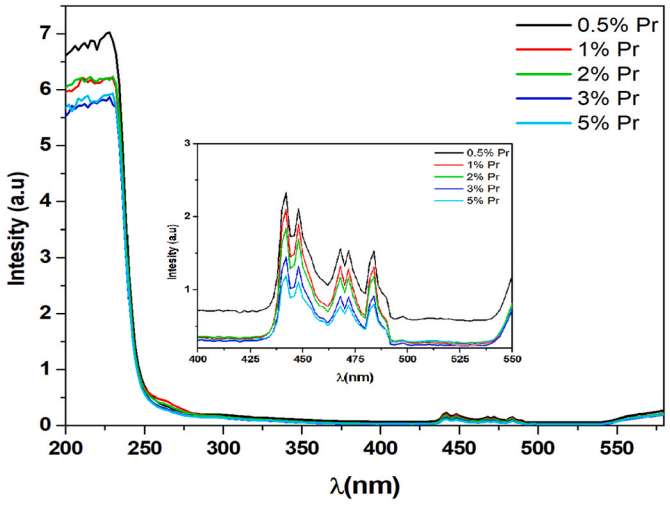

Fig. 3. PL excitation spectra of $La_{1-x}Pr_xAsO_4$ (x = 0.5 %; 1 %; 2 %; 3 % and 5 %) at room temperature.

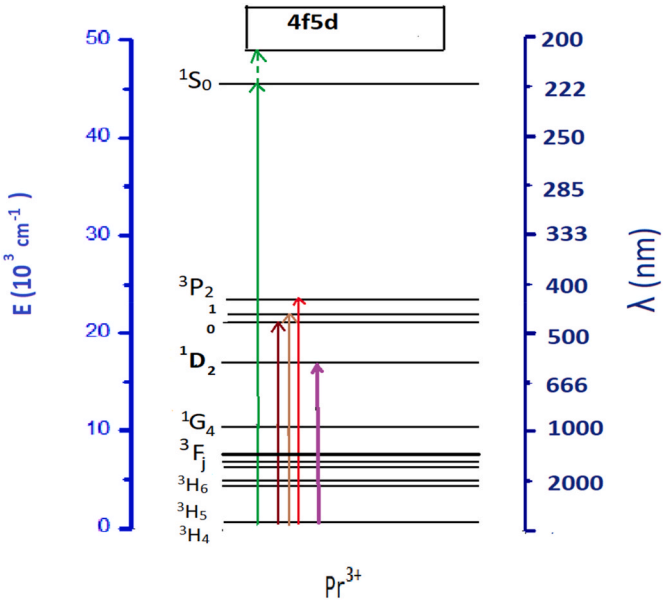

Fig. 4. Schematic energy level diagram of the Pr^{3+}.

spectrum correspond to the direct excitation of the Pr^{3+} ground condition at higher levels of the $4f^15\ d^1$-multifarious [33]. Fig. 4 presents a schematic energy level diagram of Pr^{3+}, where the cut-off edges of all Pr^{3+} doped $LaAsO_4$ samples are located in the UV (200 nm, E = 50000 cm^{-1}) and blue (550 nm, E = 18182 cm^{-1}) regions. A broad excitation band centered at 225 nm is noticed, which is attributed to the $^3H_4 \rightarrow 4f^1 5\ d^1$ transition. The several bands in the blue region from 425 to 490 nm, are imputed to $^3H_4 \rightarrow {}^3P_J$ and $^3H_4 \rightarrow {}^1D_2$, 4f-4f transitions.

According to the photon cascade excitation of Pr^{3+}, which is schematically presented in Fig. 4, the recorded bands indicate a structure of peaks that could be related to the local symmetry occupied by Pr^{3+} in $LaAsO_4$. The crystal-field interaction with the arsenic ions in its first coordination shell breaks the degeneracy of the $^{2S+1}L_J$ multiplets and leads to the formation of Stark sublevels. Therefore, these peaks are associated with transitions between the Stark sublevels of the exciting and ground levels [34].

The absorption band in the UV region is stronger than in the blue region because the Pr^{3+} $4f^2 \rightarrow 4f_15\ d^1$ transition should be fully authorized. This result could be attributed to the charge-transfer transition of oxygen to praseodymium as mentioned previously [5]. The splitting of the bands was probably because of the crystal field effects [5,34,35]. The lack of agreement between the band's intensities and Pr^{3+} concentration is proved. The relationship between the band's intensities and the concentration of the rare earth doping, in which the intensity increases with the doping rate until an optimal concentration, is established earlier in other works [36,37]. However, in this work, the intensity decreases with increasing concentration of Pr^{3+} doping, in which 0.5 % Pr^{3+} has the highest intensity. Therefore, the optimal concentration of the doping Pr^{3+} ions in $LaAsO_4$ matrix is about 0.5 %.

Fig. 5 shows the PL emission spectra of the samples recorded in the visible region from 500 to 750 nm using an excitation wavelength of λ_{ex} = 460 nm at room temperature. The spectra indicate the presence of multiple sharp emission bands associated with radiative transitions, i.e. $^1D_2$- $^3H_4$ (610 nm), $^3P_0$–$^3F_2$ (644 nm), $^3P_1$– $^3F_3$ (680 nm), $^3P_1$– $^3F_4$ (700 nm) and $^3P_0$–$^3F_4$ (725 nm).

For the system doped with 0.5 % of Pr^{3+}, the most intense peak at 610 nm is related to the red $^1D_2$-$^3H_4$ transition. The NIR ($^3P_0$– $^3F_4$ (725 nm) emission intensity is relatively weak. For the 1 %, 2 %, 3 % and 5 % content of Pr^{3+}, the intensity peaks of the red and the NIR transitions are practically similar. In other similar studies, the intensity ratio increased

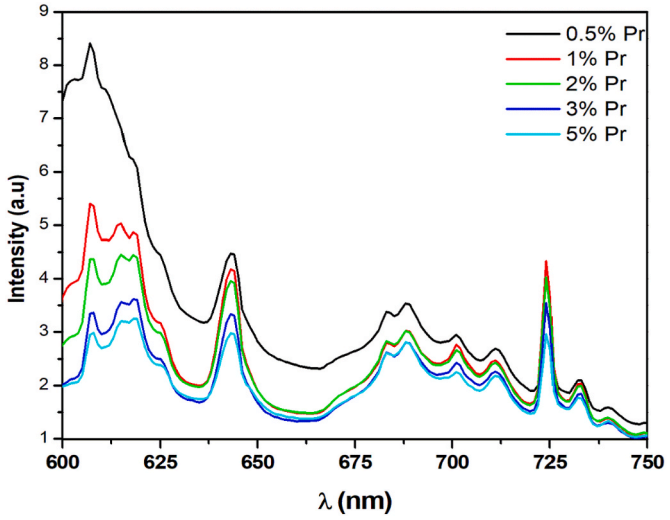

Fig. 5. PL excitation spectra of the samples $La_{1-x}Pr_xAsO_4$ (x = 0.5 %; 1 %; 2 %; 3 % and 5 %).

as the Pr^{3+} dopants increased [38,39]. However, in this work, the intensity ratio decreases as the Pr^{3+} ~~dopants~~concentration increases in agreement with previous studies [40–43]. This behavior could be due to the stronger concentration quenching of $^1D_2$ level versus the $^3P_0$ level, which is known for Pr^{3+} luminescence.

To further study the fluorescent emission of the $La_{1-x}Pr_xAsO_4$ (x = 0.5 %; 1 %; 2 %; 3 % and 5 %) samples, the decay curves at room temperature and under pulsed laser excitation (λ_{ex} = 460 nm) were measured as shown in Fig. 6. All the curves could be well fit into a single-exponential function $I(t) = I_0 \exp(-t/\tau)$ (I_0 is the initial emission intensity at t = 0 and τ is the lifetime).

The lifetimes of different samples are presented in Table 2. In the low dopant concentrations of Pr^{3+} 0.5 % and 1 %, τ = 13.5 and 13.3 μs, respectively. Then τ decreases gradually with Pr^{3+} concentration to reach 7.8 μs for 5 % of Pr^{3+}. The lifetime shortening could be explained by the probability of nonradiative interactions between dopants with the shortening of the average distance between them [44]. Considering a hypothesis that Pr^{3+} ions are randomly distributed among La^{3+} sites in the $LaAsO_4$ structure, the increase in their concentration resulted in the shortening of the average distance between them, facilitating Pr^{3+}–Pr^{3+}

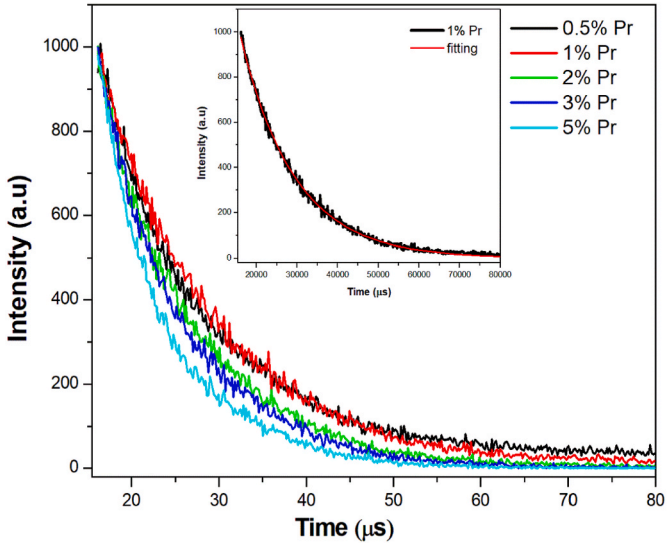

Fig. 6. Decay curves of $La_{1-x}Pr_xAsO_4$ (x = 0.5 %; 1 %; 2 %; 3 % and 5 %) (Inset: The experimental and the fitting curves of $La_{0.99}Pr_{0.01}AsO_4$).

Table 2
Variation of the lifetime as a function of the concentration of Pr^{3+}.

Pr^{3+} concentration (%)	T (μs)	R^2
0.5	13.5	0.99
1	13.3	0.99
2	10.2	0.99
3	9.6	0.99
5	7.8	0.99

energy transfer.

It could be noticed that the optimal luminescence of Pr-doped $LaAsO_4$ occurs at low Pr^{3+} concentration (0.5 %). This result is opposite from those observed in other Pr-doped materials like YAG:Pr and $LaPO_4$ [16,17] where the luminescence increased with the dopant concentrations. This suggests a particular interaction between Pr^{3+} ions and the $LaAsO_4$ matrix, involving more complex energy transfer mechanisms or enhanced quenching effects at higher concentrations. The PL emission spectra display sharp bands characteristic of Pr^{3+} transitions, with significant influence from the crystal field environment. These findings contribute to our understanding of rare-earth-doped luminescent materials but also highlight the potential for tuning material properties through careful control of doping levels, as indicated by shifts in chromaticity coordinates correlating with dopant concentration [20].

3.4. DFT calculations

3.4.1. Band structure

Fig. 7a reveals that the undoped $LaAsO_4$ adopts a monoclinic crystal structure within the $P2_1/n$ space group. The asymmetric unit of this structure comprises one lanthanum atom, one arsenic atom, and four oxygen atoms, each occupying the general position 4e. However, due to computational constraints, substitution in the structure is limited to one La atom being replaced by a Pr atom, as depicted in Fig. 7b. This substitution results in the formation of the doped compound, represented by the formula $La_{0.75}Pr_{0.25}AsO_4$.

The band structures of pure $LaAsO_4$, computed utilizing the generalized gradient approximation method (GGA-PBE), are presented for both $P2_1/n$ and P1 space groups in Fig. 8a and b, respectively. For $LaAsO_4$ with praseodymium doping ($La_{0.75}Pr_{0.25}AsO_4$), the calculations are conducted using the GGA-PBE + U scheme. This approach incorporates a Hubbard parameter (U) set at 4 eV, enhancing the depiction of correlation effects within the localized d orbitals of the praseodymium atoms. The band structures of both the undoped and Pr-doped $LaAsO_4$ are comprehensively illustrated in Fig. 8.

The optical band gap for $LaAsO_4$ is determined to be around 4.46 eV. Fig. 8a and b indicate that variations in symmetry have a minimal impact on the optical band gap of $LaAsO_4$, which continues to be a direct gap located at the gamma point within the Brillouin zone.

The band structure of undoped $LaAsO_4$ was investigated over an energy range of −20 to 10 eV. In contrast, for Pr-doped $LaAsO_4$, the range extends from −36 to 10 eV to accommodate the new energy level at −35 eV that arises due to the Pr inclusion. The band structure of $La_{0.75}Pr_{0.25}AsO_4$ is depicted in Fig. 8c and d.

As illustrated in Fig. 8c, the incorporation of Pr generates new energy levels within the forbidden band of the material. Consequently, the gap energy is reduced to approximately 2.299 eV (Fig. 8d), suggesting that the modified material exhibits optical activity within the visible spectrum, specifically in the green color range. The value of the calculated optical gap of $La_{0.75}Pr_{0.25}AsO_4$ is close to the experimental and theoretical values determined for the pure $PrAsO_4$ [30]. In the case of Pr-doped $SrSnO_3$, a decrease in the optical gap from 3.67 to 2.43 eV with a 7 % Pr doping level was noted [45]. This observation was theoretically substantiated using DFT, which yielded a similar value of 2.53 eV for the Pr-doped $SrSnO_3$ compound [45].

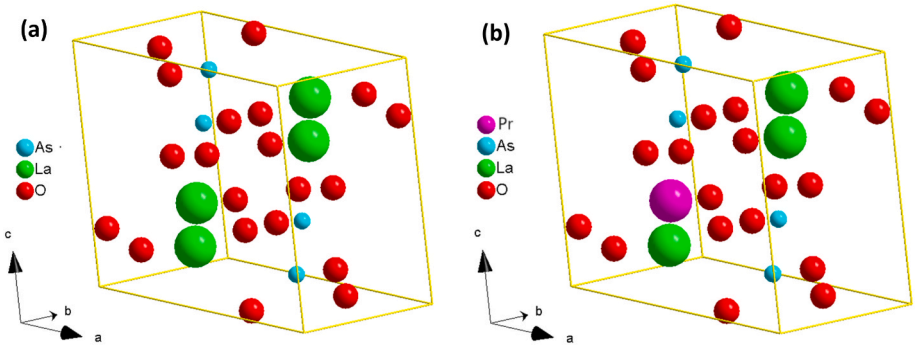

Fig. 7. Projection of the optimized unit cell of (a) $LaAsO_4$ and (b) $La_{0.75}Pr_{0.25}AsO_4$.

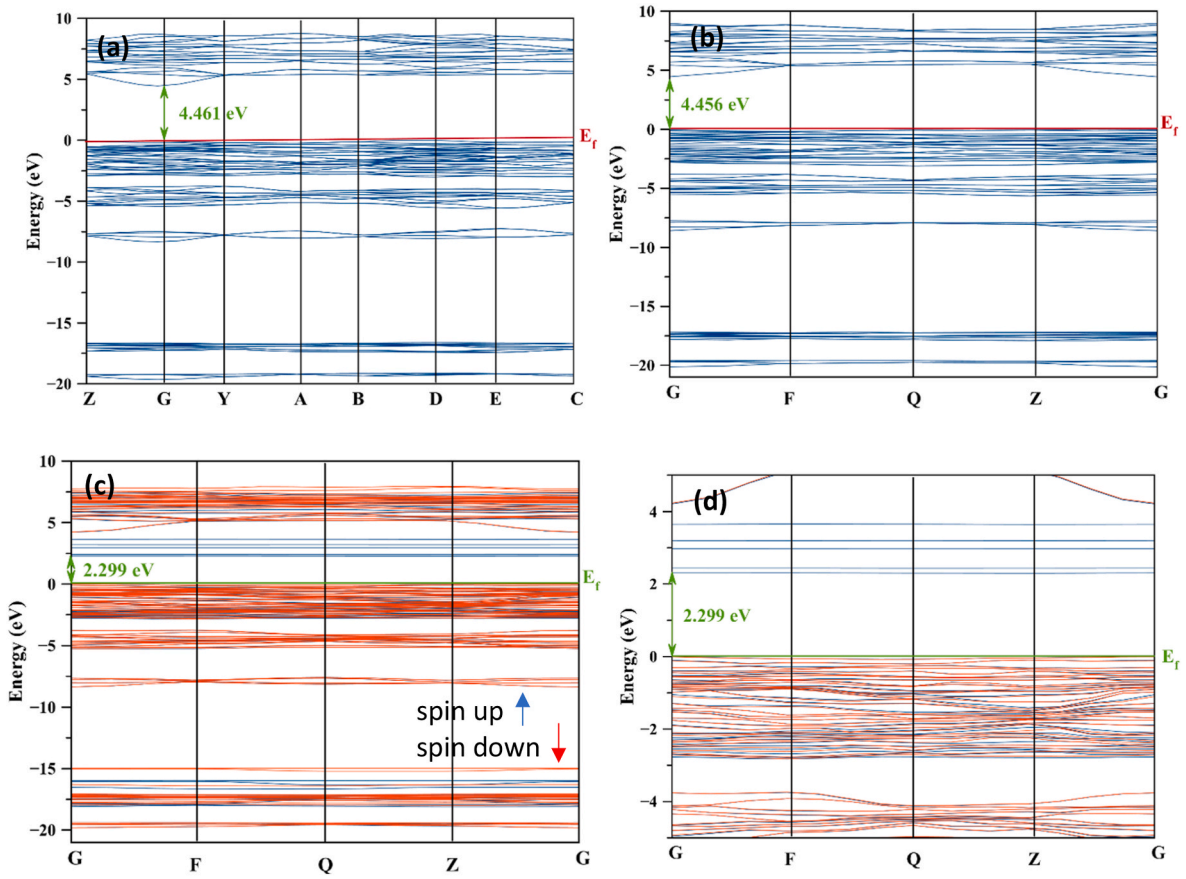

Fig. 8. The bond structure of (a) $LaAsO_4$ in $P2_1/n$ and (b) in P1 and the band structure of $La_{0.75}Pr_{0.25}AsO_4$ in an (c) overview and (d) a large view.

3.4.2. Density of states (DOS)

To determine the energy levels associated with the Praseodymium atom intercalated in the forbidden band (as illustrated in Fig. 8d) and to gain a deeper understanding of the electronic structure of both doped and undoped $LaAsO_4$. The total and partial density of states for $LaAsO_4$ and $La_{0.75}Pr_{0.25}AsO_4$ are shown in Figs. 9 and 10, respectively. The analysis covered an energy range of −22 to 10 eV for $LaAsO_4$ and -36 to 10 eV for Pr-doped $LaAsO_4$.

The DOS analysis of $LaAsO_4$ (Fig. 9) indicates that the valence states can be divided into four separate sub-bands: V1, V2, V3, and V4. The initial sub-band V1, found within the energy range of approximately −6 to 0 eV, primarily consists of O-2p states with minor contributions from As-4p and La-4d states. The subsequent sub-band V2, extending from around −6 to −10 eV, results from the hybridization of As-3s and O-2p states, with minor involvement of O-2s states, revealing significant covalent bonding characteristics between As and O atoms. The third sub-band V3, covering the energy range of −17 to −19 eV, corresponds to the hybridized O-2s and As-3p states. Lastly, the deep sub-band V4, ranging from −19 to −21 eV, emerges from As-4s and O-2s states. In $LaAsO_4$, the conduction band is composed of a single C1 band, stretching from the CBM to 10 eV. This band is primarily attributed to the La-4d state, with minor contributions from La-4p, La-4s, As-3p, and As-3d states, as demonstrated in Fig. 9. The weak contribution from As-3p and As-3d states highlights the dominant role of La in the conduction band.

Fig. 10 exhibits the total and partial density of states (DOS) for $La_{0.75}Pr_{0.25}AsO_4$, providing a comprehensive view of the electronic structure of the post-Praseodymium doping. The total DOS at the top of the figure shows significant spin polarization, indicating magnetic behaviour due to the Pr doping. The asymmetry between these states

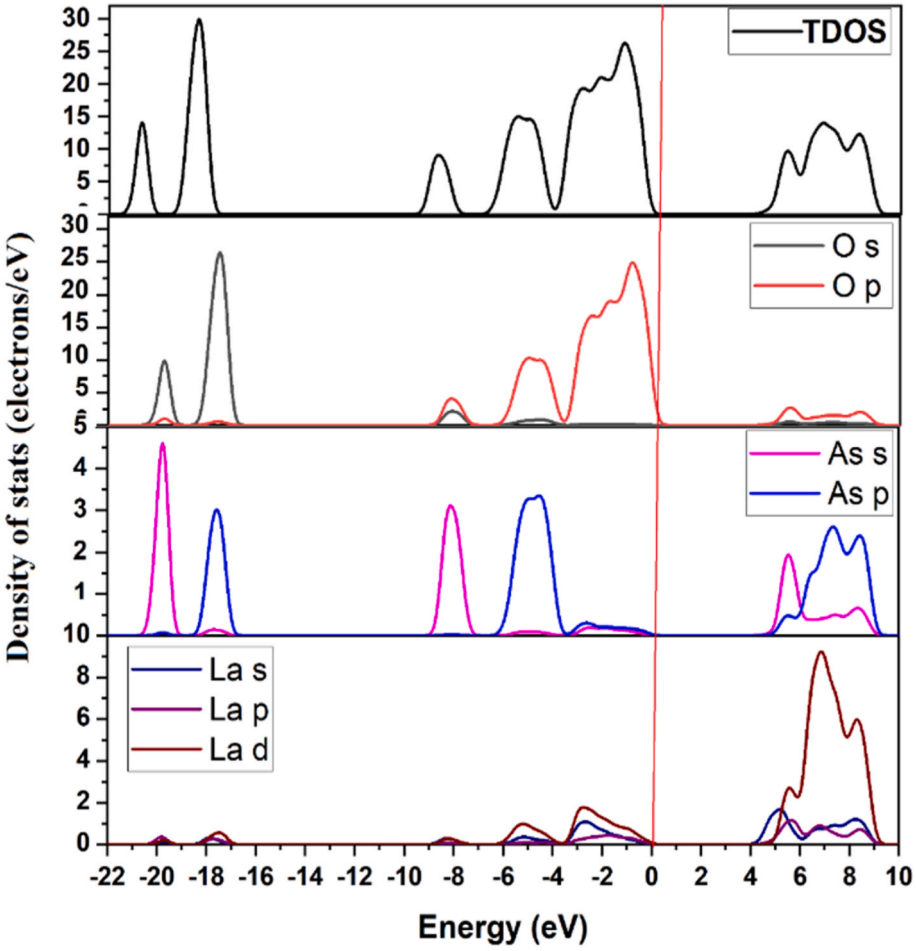

Fig. 9. Total and partial density of states of $LaAsO_4$ compound.

suggests the possibility of magnetic ordering, which is a key consideration for spintronic applications.

From the partial DOS, the f-states of Pr are conspicuously responsible for the introduction of new energy levels at −35 eV, situated within the band gap. This is an unusual feature as it implies that Praseodymium f-electrons provide localized states within the band gap that can affect the electronic transitions and optical properties of the material. The presence of these states is likely to lead to a narrowing of the band gap, as also corroborated by the data in Fig. 8d, where the band gap is reduced to approximately 2.299 eV. This narrowing brings the energy gap into the range of visible light, which implies that the material could now absorb and potentially emit light within the visible spectrum – an attribute that could be harnessed in optoelectronic devices.

The partial DOS further reveals the atomic contributions to the electronic structure: Oxygen p-states dominate the valence band near the Fermi level, while the conduction band is primarily characterized by the d-states of Lanthanum, with minor contributions from Praseodymium and other orbitals.

3.4.3. Optical properties

The dielectric function, which is essential in describing the optical properties of a material, could be expressed as a complex function of frequency [34]:

$$\varepsilon(\omega) = \varepsilon_1(\omega) + i\varepsilon_2(\omega) \tag{2}$$

Where $\varepsilon_1(\omega)$ and $\varepsilon_2(\omega)$ represents the real (dispersive) and imaginary (absorptive) parts, respectively [46]. The imaginary part $\varepsilon_2(\omega)$ could be calculated numerically by evaluating the momentum matrix elements of the electric dipole operator between the wave functions of the conduction and valence bands, according to equation (2) [47]:

$$\varepsilon_2(\omega) = \left(\frac{2e^2\pi}{\omega\varepsilon_0}\right)\sum_{kvc}\left|\langle\psi_k^c|\mathrm{u.r}|\psi_k^v\rangle\right|^2\delta\left(\mathrm{E}_k^c - \mathrm{E}_k^v - E\right) \tag{3}$$

In this equation, u represents the polarization vector of the incident electric field, r is the electron's radius vector, e is the electric charge, and ψ_k^c and ψ_k^v are the conduction and valence band wave functions at k, respectively, with ε_0 being the vacuum permittivity. The summation in equation (2) is applied over all states from the occupied and empty bands, with their wave functions obtained numerically after optimizing the crystal structure. The real part of the dielectric function, $\varepsilon_1(\omega)$, could be determined from the imaginary part using the Kramers–Krönig dispersion equation (4):

$$\varepsilon_1(\omega) = 1 + \frac{2}{\pi}p\int_0^\infty \frac{\omega'\varepsilon_2(\omega')d\omega'}{\omega'^2 - \omega^2} \tag{4}$$

Where P denotes the principal value of the integral.

Other optical properties, such as the refractive index $n(\omega)$, the extinction coefficient $k(\omega)$ and the absorption coefficient $\alpha(\omega)$ can could be derived from the real and imaginary parts of the dielectric function as follows [47]:

$$n(\omega) = \frac{\sqrt{\varepsilon_1^2(\omega) + \varepsilon_2^2(\omega)} + \varepsilon_1^2(\omega)}{\sqrt{2}} \tag{5}$$

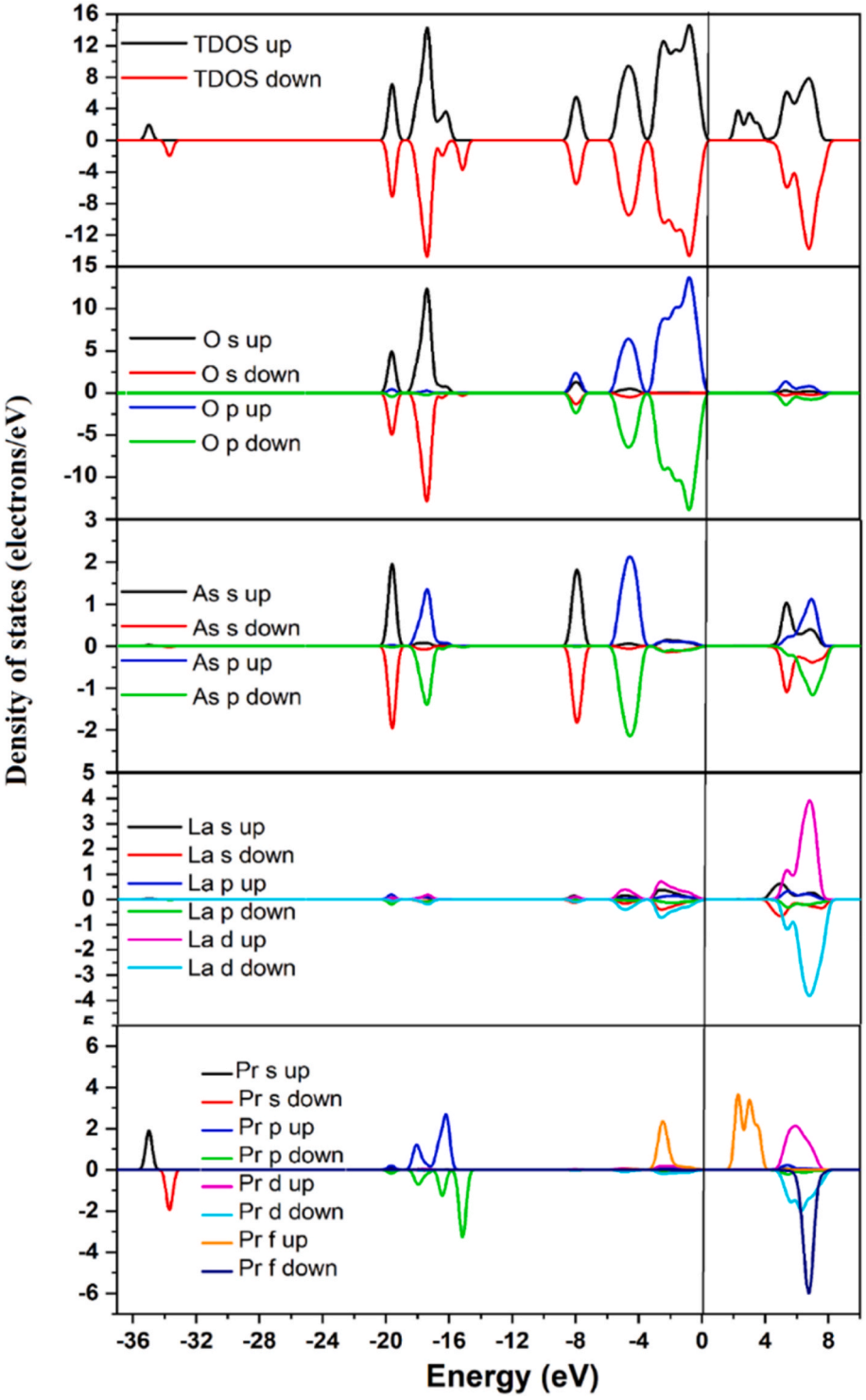

Fig. 10. Total and partial densities of states of $La_{0.75}Pr_{0.25}AsO_4$.

$$k(\omega) = \frac{\sqrt{\varepsilon_1^2(\omega) + \varepsilon_2^2(\omega)} - \varepsilon_1^{1/2}(\omega)}{\sqrt{2}} \quad (6)$$

$$\alpha(\omega) = \sqrt{2}\left[\sqrt{\varepsilon_1^2(\omega) + \varepsilon_2^2(\omega)} - \varepsilon_1(\omega)\right]^{1/2} \quad (7)$$

The dielectric function of $LaAsO_4$ and $La_{0.75}Pr_{0.25}AsO_4$ is depicted in Fig. 11, highlighting the complex optical behavior of these materials. Fig. 11a and b give an overview of the dielectric function for $LaAsO_4$ and $La_{0.75}Pr_{0.25}AsO_4$ compounds respectively across a wide energy range from 0 to 32 eV. In both compounds, the real part of the dielectric function (ε_1) starts from a positive value at zero energy, which is typical for dielectrics, indicating the presence of polarizability. The imaginary part (ε_2) starts from zero, suggesting low absorption at zero energy. As the energy increases, both ε_1 and ε_2 exhibit peaks, with ε_2 peaks representing significant absorption bands due to electronic transitions from the valence to the conduction band. Fig. 11c provides an enlarged view of the dielectric function in the lower energy range, below 4 eV, which is particularly significant for optical applications. The marked area within the red circle shows a substantial feature in the $La_{0.75}Pr_{0.25}AsO_4$

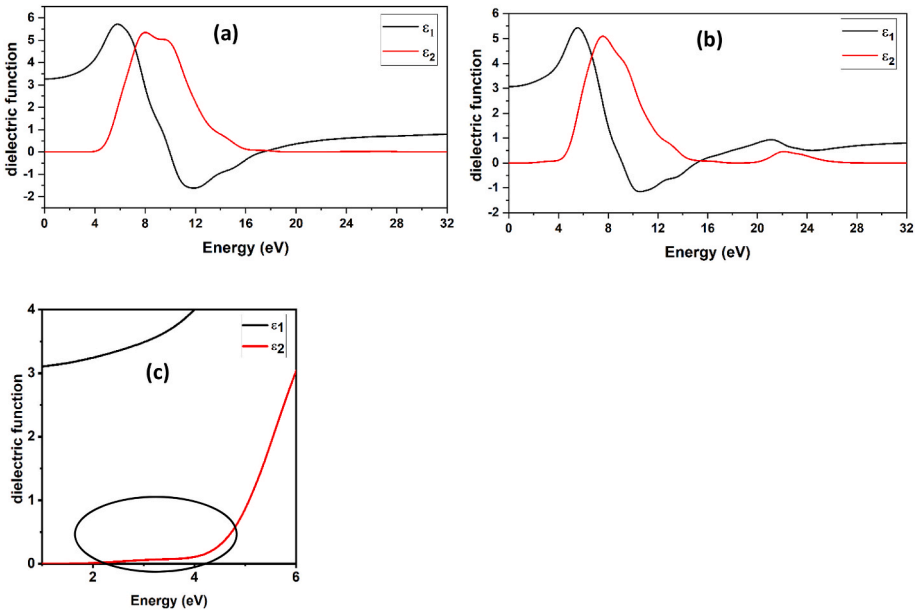

Fig. 11. Dielectric function of (a) $LaAsO_4$ and $La_{0.75}Pr_{0.25}AsO_4$ compounds (b) overview and (c) enlarged view showing the band below 4 eV.

compound, not observed in the pure $LaAsO_4$. This feature likely corresponds to the reduced band gap caused by the incorporation of Pr, as previously mentioned. The peak in the ε_2 component within this energy range suggests a strong absorption, which could be associated with the new energy levels introduced by Pr doping, that fall within the visible range. This indicates that Pr-doping enhances the material's interaction with visible light, potentially making it useful for optoelectronic applications.

The refractive index (n) and extinction coefficient (k) for both $LaAsO_4$ and $La_{0.75}Pr_{0.25}AsO_4$ are displayed in Fig. 12. These two parameters are crucial as they describe the optical properties of materials. The refractive index (n) represents the real part of the dielectric function and gives information on how much light is slowed down in the material compared to the speed of light in a vacuum. The extinction coefficient (k), representing the imaginary part, indicates the amount of light loss due to absorption and scattering when light propagates through the material.

Fig. 12a and b are the overview of these optical constants across a broad energy range, from 0 to 30 eV, for $LaAsO_4$ and $La_{0.75}Er_{0.25}AsO_4$, respectively. Both materials display a similar trend, with the refractive index starting high at lower energies and decreasing as the energy increases. Notably, there are peaks in the extinction coefficient, which corresponds to energies where the material has strong absorption due to electronic transitions.

The behavior of these optical constants below 4 eV is highlighted in Fig. 12c. The marked difference in the extinction coefficient (k) for $La_{0.75}Pr_{0.25}AsO_4$ within the low energy range is of particular interest. This indicates a higher absorption in the visible region for the Pr-doped compound, likely due to the introduction of new energy levels within the band gap as a result of Pr doping. The increase in the extinction coefficient in this region suggests the doped material could be more effective in absorbing visible light, which could be advantageous for applications in areas such as solar cells or photodetectors.

The refractive index (n) for $La_{0.75}Pr_{0.25}AsO_4$ also appears to be slightly higher than that of the undoped $LaAsO_4$ in the visible range, which could mean a higher phase velocity of light in the material,

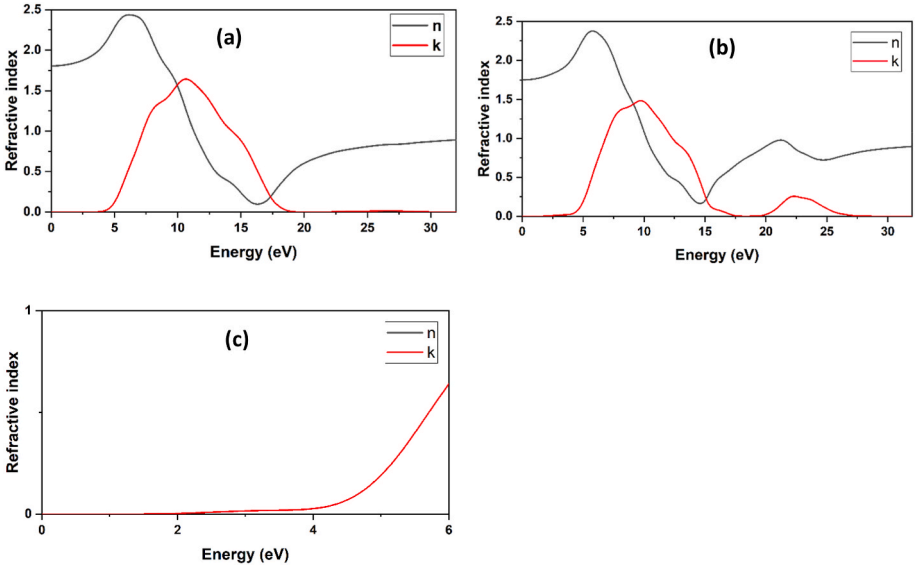

Fig. 12. Real and imaginary parts of the dielectric function of (a) $LaAsO_4$, (b) $La_{0.75}Pr_{0.25}AsO_4$and (c) enlarged view showing the band below 4 eV.

potentially affecting the design of optical devices where material dispersion is a critical factor. The higher refractive index at these energies could lead to a stronger confinement of light within the material, which is beneficial for waveguiding applications.

Fig. 13 provides the absorption spectra for $LaAsO_4$ and the Praseodymium-doped variant $La_{0.75}Pr_{0.25}AsO_4$, detailing their interaction with light across various energy levels. In Fig. 13a and b, the spectra cover an extensive energy range from 0 to 32 eV. The absorption coefficient, α(ω), quantifies how much light is absorbed over a range of photon energies, with pronounced peaks indicating significant absorption typically associated with electronic transitions from the valence to the conduction band.

For $LaAsO_4$ (Fig. 13a), a prominent absorption peak commences at approximately 4.5 eV and reaches a peak around 12 eV with an intensity of about 300000 cm^{-1}, indicating strong UV absorption. This peak intensity then tapers off with increasing energy, with another less intense peak surfacing near 20 eV. A secondary, less pronounced peak is observed around 25 eV. This pattern suggests that $LaAsO_4$ absorbs strongly in the UV range, with relatively lower absorption in the visible spectrum. The absorption spectrum of $La_{0.75}Pr_{0.25}AsO_4$, shown in Fig. 13b, exhibits a peak in the UV range as well, yet the profile is distinctly altered due to Pr doping. The peak's maximum intensity is reduced to below 250000 cm^{-1}, while the intensity of a second peak at higher energy levels increases to approximately 10000 cm^{-1}. These variations indicate that Pr doping modifies the electronic structure, thereby altering the absorption characteristics of the material.

Furthermore, Fig. 13c highlights a small but noticeable peak between 2 and 4 eV, attributed to the introduction of the Pr f-states within the band gap. The emergence of this peak suggests absorption in the lower energy range, signifying that the optical band gap is reduced, enabling absorption within the visible spectrum. The variation in intensity from the undoped to the Pr-doped $LaAsO_4$ could be ascribed to the additional energy levels that are introduced by the Pr doping. These new levels alter the electronic transitions that contribute to the absorption spectrum, as evidenced by the changes in peak intensities and the appearance of new absorption features in the visible range. The Pr f-states are responsible for the additional absorption peak, which corroborates the previously discussed effects of Pr doping on the material's optical band gap and electronic structure.

Fig. 13c further provides an enlarged view of the absorption spectrum below 6 eV, which is crucial for applications involving visible light. The spectrum for $La_{0.75}Pr_{0.25}AsO_4$ shows absorption beginning at lower energies compared to $LaAsO_4$. This suggests that the Pr-doped material has a narrower band gap, which is consistent with the previously noted band structure and dielectric function analyses. The onset of absorption in the visible range indicates that $La_{0.75}Pr_{0.25}AsO_4$ could be more effective in absorbing visible light, which is advantageous for optoelectronic applications such as light-emitting diodes (LEDs). The enhanced absorption in the visible range for the Pr-doped material could be attributed to the introduction of Pr-related energy levels within the band gap, facilitating new electronic transitions that are not possible in the undoped compound. This aligns with the expected modification of optical properties due to the presence of Pr, potentially making $La_{0.75}Pr_{0.25}AsO_4$ a promising material for optical applications.

The DFT calculations provided deep insights into the electronic structure modification induced by Pr doping. In fact, our findings show a substantial reduction in the optical band gap with Pr incorporation, facilitating the absorption and emission in the visible spectrum. This theoretical prediction is validated by the experimental observations of enhanced visible light emission. Furthermore, the use of GGA + PBE and GGA + PBE + U approximations elucidates the interaction of Pr's 4f states with the host lattice, which is critical for understanding the photoluminescence behavior.

4. Conclusions

$La_{1-x}Pr_xAsO_4$ with varying concentrations of Pr^{3+} synthesized via the combustion method has provided significant insights into the optoelectronic properties of this material. XRD analysis has confirmed the preservation of the pure, monoclinic crystal structure across all doping levels, with crystallite sizes consistently ranging from 60 to 76 nm. The SEM analysis has revealed a homogeneous distribution of irregularly shaped particles irrespective of the Pr^{3+} concentration. The optoelectronic evaluation has highlighted the material's strong absorption in the UV and blue regions and its distinct emission peaks in the visible spectrum, especially at 610 nm, with the most intense luminescence occurring at a Pr^{3+} doping level of 0.5 %. This outcome of the current study is particularly noteworthy as it contradicts the typical trend of increasing luminescence with dopant concentration, indicating a unique interaction between the Pr^{3+} ions and the $LaAsO_4$ matrix. The DFT calculations have revealed the introduction of Pr's 4f states into the $LaAsO_4$ forbidden band, which has led to a substantial reduction in the optical band gap and corroborates the visible light emissions recorded. Our findings provide a deep understanding of Pr-doped $LaAsO_4$, emphasizing the utility of theoretical approaches in predicting and analyzing their optoelectronic properties.

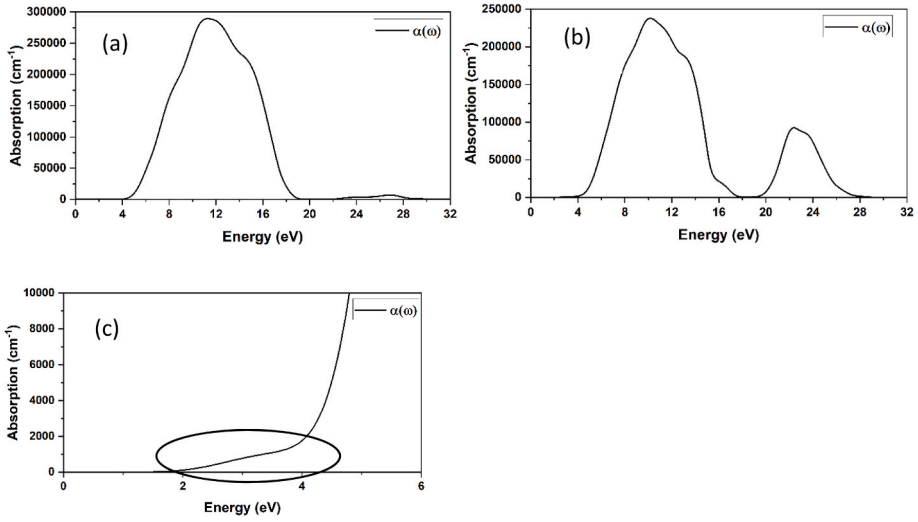

Fig. 13. Absorption spectrum of (a) $LaAsO_4$ and $La_{0.75}Pr_{0.25}AsO_4$ (b) overview and (c) enlarged view.

CRediT authorship contribution statement

Basma Marzougui: Formal analysis, Software, Writing – original draft. **Youssef Ben Smida:** Investigation, Methodology, Software, Writing – original draft, Writing – review & editing. **Mounir Ferhi:** Formal analysis, Validation, Visualization. **Hela Ferjani:** Formal analysis, Writing – original draft. **Damian Onwudiwe:** Writing – review & editing. **Ahmed Hichem Hamzaoui:** Writing – review & editing. **Mohamed Triki:** Writing – review & editing. **Y. Al Douri:** Writing – review & editing.

Declaration of competing interest

The authors declare that they have no known competing financial interests or personal relationships that could have appeared to influence the work reported in this paper.

References

[1] O. AitMellal, L. Oufni, M. Messous, M. Tahri, Ş. Neatu, M. Florea, F. Neatu, M. Secu, Structural properties and near-infrared light from Ce^{3+}/Nd^{3+}-co-doped $LaPO_4$ nanophosphors for solar cell applications, J. Mater. Sci. Mater. Electron. 33 (2022) 4197–4210.

[2] Y. Kumar, S. Tripathi, M. Nand, R. Jangir, V. Srihari, A. Das, R. Singh, U. Deshpande, S. Jha, A. Arya, Structural and optical properties of Nd doped $LaPO_4$, J. Alloys Compd. 925 (2022) 166772.

[3] N. Saltmarsh, G. Kumar, M. Kailasnath, V. Shenoy, C. Santhosh, D. Sardar, Spectroscopic characterizations of Er doped $LaPO_4$ submicron phosphors prepared by homogeneous precipitation method, Opt. Mater. 53 (2016) 24–29.

[4] R. Priya, R. Mariappan, A. Karthikeyan, E. Palani, E. Krishnamoorthy, G. Gowrisankar, Review on rare earth metals doped $LaPO_4$ for optoelectronic applications, Solid State Commun. 339 (2021) 114457.

[5] Z. Xiu, S. Liu, M. Lü, H. Zhang, G. Zhou, Photoluminescence of Eu^{3+}-doped $LaPO_4$ nanocrystals synthesized by combustion method, Mater. Res. Bull. 41 (2006) 642–646.

[6] N. Adala, B. Marzougui, Y.B. Smida, R. Marzouki, M. Ferhi, D.C. Onwudiwe, A. H. Hamzaoui, An experimental and theoretical study of the structural, optical, electrical, and dielectric properties of $PrAsO_4$, J. Alloys Compd. 910 (2022) 164894.

[7] M. Huse, T. Norby, R. Haugsrud, Proton conductivity in acceptor-doped $LaVO_4$, J. Electrochem. Soc. 158 (2011) B857.

[8] T. Norby, N. Christiansen, Proton conduction in Ca-and Sr-substituted $LaPO_4$, Solid State Ionics 77 (1995) 240–243.

[9] C.J. Van Hoozen, A.P. Gysi, D.E. Harlov, The solubility of monazite ($LaPO_4$, $PrPO_4$, $NdPO_4$, and $EuPO_4$) endmembers in aqueous solutions from 100 to 250 C, Geochem. Cosmochim. Acta 280 (2020) 302–316.

[10] D. Errandonea, O. Gomis, P. Rodríguez-Hernández, A. Muñoz, J. Ruiz-Fuertes, M. Gupta, S. Achary, A. Hirsch, F.-J. Manjón, L. Peters, High-pressure structural and vibrational properties of monazite-type $BiPO_4$, $LaPO_4$, $CePO_4$, and $PrPO_4$, J. Phys. Condens. Matter 30 (2018) 065401.

[11] K. Toyoura, K. Matsunaga, Hydrogen bond dynamics in proton-conducting lanthanum arsenate, J. Phys. Chem. C 117 (2013) 18006–18012.

[12] T.S. Bjørheim, T. Norby, R. Haugsrud, Hydration and proton conductivity in $LaAsO_4$, J. Mater. Chem. 22 (2012) 1652–1661.

[13] M.H.N. Thi, N.T.P. Loan, N.D.Q. Anh, Study of red-emitting $LaAsO_4:Eu^{3+}$ phosphor for color rendering index improvement of WLEDs with dual-layer remote phosphor geometry, TELKOMNIKA (Telecommunication Computing Electronics and Control) 18 (2020) 3210–3215.

[14] N. Loan, N. Anh, Enhancing optical performance of dual-layer remote phosphor structures with the application of $LaAsO_4$: Eu^{3+} and $Y_2O_3:Ho^{3+}$, Optoelectronics and, Adv. Mater.-Rapid Commun. 15 (2021) 71–78.

[15] S. Hu, C. Lu, X. Liu, Z. Xu, Optical temperature sensing based on the luminescence from YAG: Pr transparent ceramics, Opt. Mater. 60 (2016) 394–397.

[16] M. Wisniewska, D. Wisniewski, A. Wojtowicz, S. Tavernier, T. Lukasiewicz, Z. Frukacz, Z. Galazka, M. Malinowski, Luminescence and scintillation properties of YAG:Pr. 2001 IEEE Nuclear Science Symposium Conference Record (Cat. No. 01CH37310), IEEE, 2001, pp. 341–345.

[17] T. Malyy, V. Vistovskyy, Z. Khapko, A. Pushak, N. Mitina, A. Zaichenko, A. Gektin, A. Voloshinovskii, Recombination luminescence of $LaPO_4$-Eu and $LaPO_4$-Pr nanoparticles, J. Appl. Phys. 113 (2013).

[18] L. Macalik, P.E. Tomaszewski, A. Matraszek, I. Szczygieł, P. Solarz, P. Godlewska, M. Sobczyk, J. Hanuza, Optical and structural characterisation of pure and Pr^{3+} doped $LaPO_4$ and $CePO_4$ nanocrystals, J. Alloys Compd. 509 (2011) 7458–7465.

[19] L.-G. Teoh, H.-L. Chen, S. Wu, C.-R. Chang, Y.-S. Chang, Characteristics of Pr^{3+} ion-doped t-zircon type $LaVO_4$ prepared using a hydrothermal method, J. Electroceram. (2021) 1–6.

[20] H.-L. Chen, L.-K. Wei, Y.-S. Chang, Characterizations of Pr^{3+} ion-doped $LaVO_4$ phosphor prepared using a sol–gel method, J. Electron. Mater. 47 (2018) 6649–6654.

[21] X. Liu, G. Tan, Z. Zhou, W. Li, Y. Yang, Z. Sun, B. Mei, Effect of Pr^{3+} doping concentration on microstructure and optical properties of transparent BaF_2 ceramics, J. Alloys Compd. 895 (2022) 162623.

[22] Z. Li, Y.-n. Wang, K.-y. Wu, Y.-p. Xu, J. Cao, Y.-f. Wang, L. Deng, Preparation and performance of $SrWO_4$: RE^{3+} (RE= Eu, Sm, Pr) fluorescent powders for white leds, J. Appl. Spectrosc. 90 (2023) 723–729.

[23] F. Chun, W. Li, B. Zhang, W. Deng, X. Chu, H. Su, H. Osman, H. Zhang, X. Zhao, W. Yang, Visible and near-infrared luminescent properties of Pr3+ doped strontium molybdate thin films by a facile polymer-assisted deposition process, J. Colloid Interface Sci. 531 (2018) 181–188.

[24] D. Bahadur, S. Rajakumar, A. Kumar, Influence of fuel ratios on auto combustion synthesis of barium ferrite nano particles, J. Chem. Sci. 118 (2006) 15–21.

[25] T. Anuradha, S. Ranganathan, T. Mimani, K. Patil, Combustion synthesis of nanostructured barium titanate, Scripta Mater. 44 (2001) 2237–2241.

[26] S.J. Clark, M.D. Segall, C.J. Pickard, P.J. Hasnip, M.I. Probert, K. Refson, M. C. Payne, First principles methods using CASTEP, Z. für Kristallogr. - Cryst. Mater. 220 (2005) 567–570.

[27] S. Grimme, Semiempirical GGA-type density functional constructed with a long-range dispersion correction, J. Comput. Chem. 27 (2006) 1787–1799.

[28] M. Ernzerhof, G.E. Scuseria, Assessment of the perdew–burke–ernzerhof exchange-correlation functional, J. Chem. Phys. 110 (1999) 5029–5036.

[29] B. Himmetoglu, A. Floris, S. De Gironcoli, M. Cococcioni, Hubbard-corrected DFT energy functionals: the LDA+ U description of correlated systems, Int. J. Quant. Chem. 114 (2014) 14–49.

[30] N. Adala, B. Marzougui, Y.B. Smida, R. Marzouki, M. Ferhi, D.C. Onwudiwe, A. H. Hamzaoui, An experimental and theoretical study of the structural, optical, electrical, and dielectric properties of $PrAsO_4$, J. Alloys Compd. (2022) 164894.

[31] M.P. Motaung, J.O. Adeyemi, Y.B. Smida, H. Ferjani, M.M. Kabanda, D. C. Onwudiwe, E. Hosten, Synthesis, structural, and DFT studies of Cu(II) dithiocarbamate complexes, J. Mol. Struct. 1271 (2023) 133988.

[32] D.C. Liu, J. Nocedal, On the limited memory BFGS method for large scale optimization, Math. Program. 45 (1989) 503–528.

[33] K. Riwotzki, H. Meyssamy, A. Kornowski, M. Haase, Liquid-phase synthesis of doped nanoparticles: colloids of luminescing $LaPO_4$:Eu and $CePO_4$:Tb particles with a narrow particle size distribution, J. Phys. Chem. B 104 (2000) 2824–2828.

[34] M. Runowski, P. Woźny, I.R. Martín, V. Lavín, S. Lis, Praseodymium doped $YF_3:Pr^{3+}$ nanoparticles as optical thermometer based on luminescence intensity ratio (LIR)–Studies in visible and NIR range, J. Lumin. 214 (2019) 116571.

[35] M. Runowski, A. Shyichuk, A. Tyminski, T. Grzyb, V. Lavín, S. Lis, Multifunctional optical sensors for nanomanometry and nanothermometry: high-pressure and high-temperature upconversion luminescence of lanthanide-doped phosphates-$LaPO_4$/$YPO_4:Yb^{3+}$–Tm^{3+}, ACS Appl. Mater. Interfaces 10 (2018) 17269–17279.

[36] Z. Qiu, T. Luo, J. Zhang, W. Zhou, L. Yu, S. Lian, Effectively enhancing blue excitation of red phosphor Mg_2TiO_4: Mn^{4+} by Bi^{3+} sensitization, J. Lumin. 158 (2015) 130–135.

[37] W. Li, J. Lee, Microwave-assisted Sol− Gel synthesis and photoluminescence characterization of $LaPO_4$: Eu^{3+}, Li^+ nanophosphors, J. Phys. Chem. C 112 (2008) 11679–11684.

[38] Y. Ji, J. Cao, Z. Zhu, J. Li, Y. Wang, C. Tu, Luminescence properties and white emission in Pr3+ doped hexagonal $YAlO_3$ nanophosphors, Materials Express 1 (2011) 231–236.

[39] Y. Liu, J. Ren, Y. Tong, T. Wang, W. Xu, G. Chen, Observation of intra-and inter-configurational luminescence of Pr^{3+}-doped strontium phosphate glasses, J. Am. Ceram. Soc. 95 (2012) 41–44.

[40] L. Wang, X. Zhang, Z. Hao, Y. Luo, J. Zhang, X.-j. Wang, Interionic energy transfer in $Y_3Al_5O_{12}$: Ce^{3+}, Pr^{3+} phosphor, J. Appl. Phys. 108 (2010) 093515.

[41] S. Chawla, N. Kumar, H. Chander, Broad yellow orange emission from $SrAl_2O_4:Pr^{3+}$ phosphor with blue excitation for application to white LEDs, J. Lumin. 129 (2009) 114–118.

[42] H. Chen, R. Lian, M. Yin, L. Lou, W. Zhang, S. Xia, J.-C. Krupa, Luminescence concentration quenching of 1D2 state in YPO_4: Pr^{3+}, J. Phys. Condens. Matter 13 (2001) 1151.

[43] E. Van der Kolk, P. Dorenbos, C. Van Eijk, Vacuum ultraviolet excitation of 1S0 and 3P0 emission of Pr^{3+} in $Sr_{0.7}La_{0.3}Al_{11.7}Mg_{0.3}O_{19}$ and SrB_4O_7, J. Phys. Condens. Matter 13 (2001) 5471.

[44] K. Trejgis, K. Maciejewska, A. Bednarkiewicz, L. Marciniak, Near-infrared-to-near-infrared excited-state absorption in $LaPO_4:Nd^{3+}$ nanoparticles for luminescent nanothermometry, ACS Appl. Nano Mater. 3 (2020) 4818–4825.

[45] H. Shaili, E. Salmani, M. Beraich, M.h. Taibi, M. Rouchdi, H. Ez-Zahraouy, N. Hassanain, A. Mzerd, Unraveling the microstructural and optoelectronic properties of solution-processed Pr-doped $SrSnO_3$ perovskite oxide thin films, RSC Adv. 11 (2021) 37019–37028.

[46] M. Gajdoš, K. Hummer, G. Kresse, J. Furthmüller, F. Bechstedt, Linear optical properties in the projector-augmented wave methodology, Phys. Rev. B 73 (2006) 045112.

[47] Y. Peter, M. Cardona, Fundamentals of Semiconductors: Physics and Materials Properties, Springer Science & Business Media, 2010.